

Photoelectrocatalysis

Photoelectrocatalytic Degradation Mechanism of Fluorinated Pollutants Using a Bilayer WO₃ Photoanode: Synergistic Role of Holes and Hydroxyl Radicals

Qiuling Ma, Dongfeng Li, Fujun Ren, Wensheng Gao, Rui Song, Zelong Li,* and Can Li*

Abstract: Fluorinated organic pollutants pose significant environmental and health risks due to the high stability of C–F bonds, necessitating effective strategies for their degradation. Herein, we present a bilayer WO₃ photoelectrode (double-WO₃) incorporating an electron transport layer (ETL) and a hexagonal-monoclinic heterophase junction for PEC degradation of fluorinated pollutants. The double-WO₃ catalyst achieves a high photocurrent density (4.3 mA cm⁻² at 1.2 V_{RHE}) and nearly complete degradation (99.9%) of bisphenol AF (BPAF), 4-fluorophenol (4-FP), and pentafluorophenol (PFP), with 99.9% mineralization of PFP. Experimental and transient photocurrent (TPC) analyses confirm that the ETL-heterophase junction structure enhances electron extraction and surface reaction kinetics while minimizing electron-hole recombination. In this process, photogenerated h⁺ excites fluorinated pollutants, enhancing C–F bond susceptibility to •OH attack, which facilitates bond cleavage and subsequent oxidation into CO₂, H₂O, and F⁻. This study offers a promising strategy for designing advanced PEC systems and effectively remediating persistent fluorinated contaminants.

Introduction

Fluorinated organic pollutants, widely used as synthetic intermediates in pharmaceuticals, pesticides, and personal

care products, pose long-term environmental and health risks, making them a growing concern. Their high carbon–fluorine (C–F) bond energy (485 kJ mol⁻¹) significantly exceeds that of carbon–chlorine (328 kJ mol⁻¹) and carbon–hydrogen bonds (414 kJ mol⁻¹), making degradation particularly challenging.^[1,2] Thus, effective decomposition strategies must focus on breaking C–F bonds with lower energy barriers. Notably, fluorinated molecules are more prone to C–F bond cleavage in the excited state than in the ground state, generating F⁻ or radical intermediates.^[3–5] Therefore, promoting target molecules to the excited state could be a viable approach for defluorination. Thus, developing efficient strategies for fluorinated compound activation, C–F bond cleavage, and pollutant decomposition is crucial for environmental remediation.^[6]

The PEC oxidation process, which generates both photo-generated holes (h⁺) and reactive oxygen species (ROS), offers a promising solution by simultaneously promoting fluorinated molecules to their excited state and facilitating C–F bond cleavage.^[7–10] Upon photoirradiation, electron-hole pairs form in the semiconductor, and h⁺ at the photoanode activates fluorinated molecules, enhancing C–F bond cleavage, making PEC highly promising for fluoride wastewater treatment.^[11–13] Therefore, enhancing electron-hole separation and minimizing charge carrier recombination in the PEC process are essential for increasing h⁺ and ROS generation, necessitating further optimization of the photoanode catalyst.^[14–17]

To improve electron-hole separation efficiency in PEC system, employing heterophase junctions in polymorphic semiconductor-based PEC processes, such as anatase-rutile TiO₂ and α - β Ga₂O₃, has proven to be an effective strategy.^[18–22] We previously showed that monoclinic-hexagonal WO₃ promotes charge separation and transfer, thereby enhancing PEC degradation of BPA.^[18–22] However, conventional PEC systems often suffer from severe charge recombination at the surface of photoanode, which limits the h⁺ utilization efficiency.^[23–25] To address these challenges, further structural optimizations of the photoanode are needed. Building on previous research, optimizing the substrate-electrode interface by incorporating an inorganic material as an electron transport layer (ETL) can facilitate faster electron transfer to the conductive substrate and suppress charge recombination at the photoanode surface.^[26–29] WO₃, known for its high electrical conductivity, is frequently employed as an ETL in semiconductor photoanodes, such as those formed with α -Fe₂O₃ and BiVO₄, to enhance electron

[*] Q. Ma, F. Ren, W. Gao, R. Song, Z. Li, C. Li

Key Laboratory of advanced catalysis, Gansu Province, State Key Laboratory of Applied Organic Chemistry, College of Chemistry and Chemical Engineering, Lanzhou University, Lanzhou, Gansu 730000, China

E-mail: lizl@lzu.edu.cn
canli@dicp.ac.cn

D. Li, C. Li

State Key Laboratory of Catalysis, Dalian Institute of Chemical Physics, Chinese Academy of Sciences, Dalian National Laboratory for Clean Energy, Dalian, Liaoning 116023, China

Q. Ma

College of Natural Resources and Environment, Northwest A&F University, Yangling, Shaanxi 712100, China

Additional supporting information can be found online in the Supporting Information section

extraction and mitigate charge recombination.^[30–33] Therefore, rationally designing a bilayer photoanode catalyst by integrating a heterophase junction and ETL can significantly improve charge separation efficiency, inhibit surface charge recombination, enhance hole utilization, promote fluorinated molecules activation, and boost ROS production.^[34,35]

Herein, we have developed a functional bilayer WO₃-based photoelectrode (double-WO₃) that is incorporated with the ETL and heterophase junction, showing superior PEC performances. It achieves the highest photocurrent density of ca. 4.3 mA cm⁻² at 1.2 V_{RHE}, complete degradation (99.9%) of BPAF, 4-FP, and PFP, and nearly total mineralization (99.9%) of PFP within 150 min, much higher than ever reported. The exceptional degradation efficiency of fluorinated pollutants stems from the structural advantages of double-WO₃, where the ETL and heterophase junction facilitate rapid electron extraction and enhance surface reaction kinetics, effectively minimizing electron-hole recombination. In this process, the increased availability of h⁺ promotes the activation of fluorinated pollutants to their excited state, while ROS such as •OH further facilitate C–F bond cleavage, reducing the accumulation of persistent intermediates and ultimately enabling the efficient degradation of fluorinated pollutants. This work advances bilayer photoelectrode design by leveraging ETL and heterophase junctions to enhance PEC performance, offering an efficient strategy for fluorinated pollutant degradation and mineralization in environmental remediation.

Results and Discussion

A straightforward two-step fabrication process for the bilayer WO₃ photoelectrode (double-WO₃), incorporating an ETL as the inner layer and a WO₃ phase junction as the outer layer, is depicted in Figure 1a. Specifically, monoclinic WO₃ nanoflakes are grown on the W mesh through direct anodic oxidation of the W mesh to generate the inner layer (in-WO₃).^[36] Subsequently the mixed phases of monoclinic and hexagonal WO₃ are synthesized via hydrothermal process to form the outer layer (out-WO₃).^[8,37]

The crystal structures of WO₃-based photoelectrodes were analyzed using X-ray diffraction (XRD). As shown in Figure 1b, in-WO₃ exhibits a monoclinic phase (JCPDS No. 75-2187) with characteristic peaks at 23.1°, 23.6°, and 24.4°, corresponding to the (002), (020), and (200) facets, respectively. In contrast, out-WO₃ displays a mixture of monoclinic (JCPDS No. 71-2141) and hexagonal (JCPDS No. 71-2141) phases, indicating the coexistence of both WO₃ phases in the outer layer.^[33] The double-WO₃ electrode retains this mixed-phase structure, though the hexagonal WO₃ peaks appear weakened, suggesting its lower proportion in the overall sample. To further confirm the phase composition, Raman spectroscopy was conducted (Figure 1c). The spectra of in-WO₃ match well with the monoclinic phase, while out-WO₃ exhibits six Raman bands: peaks at 270, 326, 714, and 809 cm⁻¹ correspond to monoclinic WO₃, whereas peaks at 251 and 690 cm⁻¹ are attributed to hexagonal WO₃.^[38] The double-WO₃ electrode exhibits Raman signals similar

to out-WO₃, confirming the coexistence of both monoclinic and hexagonal phases. To determine the depth distribution of these phases, Raman spectroscopy was performed with different laser excitation wavelengths (325, 473, and 532 nm), considering that scattering intensity follows $I \propto (1/\lambda)^4$.^[39] As shown in Figure 1c, the Raman peaks of double-WO₃ obtained using a 325 nm laser match those excited at 473 and 532 nm, with hexagonal WO₃ peaks becoming more prominent at shorter wavelengths. XPS analysis confirmed the coexistence of W⁶⁺ and W⁵⁺ species in double-WO₃ (Figure S1). The above results suggest that the hexagonal WO₃ phase is primarily localized in the outer region, while the monoclinic phase dominates the bulk of the double-WO₃ electrode.

The scanning electron microscopy (SEM) image of the in-WO₃ photoelectrode (Figure S2a) reveals uniformly grown WO₃ nanoflakes on the W mesh with an approximate thickness of 1.8 μm. These nanoflakes exhibit well-developed facets, forming square nanosheets with an average length of ~1.75 μm and a thickness of ~95.6 nm (Figure S2b). High-resolution transmission electron microscopy (HR-TEM) further confirms the crystallographic nature of in-WO₃, where lattice spacings of 0.365 and 0.377 nm correspond to the (200) and (020) planes of monoclinic WO₃, respectively (Figure S3). For double-WO₃, the deposition of the out-WO₃ layer onto WO₃ nanoflakes results in the formation of a dense 3D WO₃ film on the outer surface of the W mesh, increasing the total electrode thickness to ~2.5 μm (Figure S4). As shown in Figure 1d, uniform nanoplates (300–500 nm) are randomly distributed on the surface of in-WO₃ nanoflakes. The HR-TEM image of double-WO₃ (Figures 1e and S5) clearly reveals the interface between in-WO₃ and out-WO₃, demonstrating intimate contact between the two layers. Based on these characterization results, it is confirmed that the inner layer consists of monoclinic WO₃ nanoflakes, while the outer layer comprises a hexagonal-monoclinic WO₃ mixed phase.

DFT calculations (Figure 1f–h) reveal that double-WO₃ exhibits increased DOS near the VBM and CBM compared to in-WO₃ and out-WO₃, promoting carrier transport and faster diffusion kinetics. The valence band edge of double-WO₃ shifts positively, indicating stronger oxidation ability of photogenerated h⁺. Additionally, its moderate d-band center ($\epsilon_d = -1.125$ eV) suggests optimized intermediate adsorption, contributing to enhanced PEC performance.

Figure 2a presents the photocurrent density–potential (*J*–*V*) curves of the as-prepared WO₃ photoelectrodes, measured in 0.1 M Na₂SO₄ under light illumination. Notably, the double-WO₃ electrode achieves a photocurrent density of approximately 4.3 mA cm⁻² at 1.2 V_{RHE}, which is 1.2 and 3.9 times higher than that of out-WO₃ (3.6 mA cm⁻²) and in-WO₃ (1.1 mA cm⁻²), respectively. Compared with out-WO₃, the significantly elevated photocurrent plateau of double-WO₃, attributed to the intercalation of ETL, indicates a higher charge carrier density. Additionally, double-WO₃ exhibits the most negative onset potential shift among all samples, suggesting superior reactivity. These results highlight the crucial role of the ETL in enhancing the photocurrent density, demonstrating that the bilayer structure effectively improves overall PEC performance.^[40] Electrochemical impedance spectroscopy (EIS) under light illumination (Figure S6)

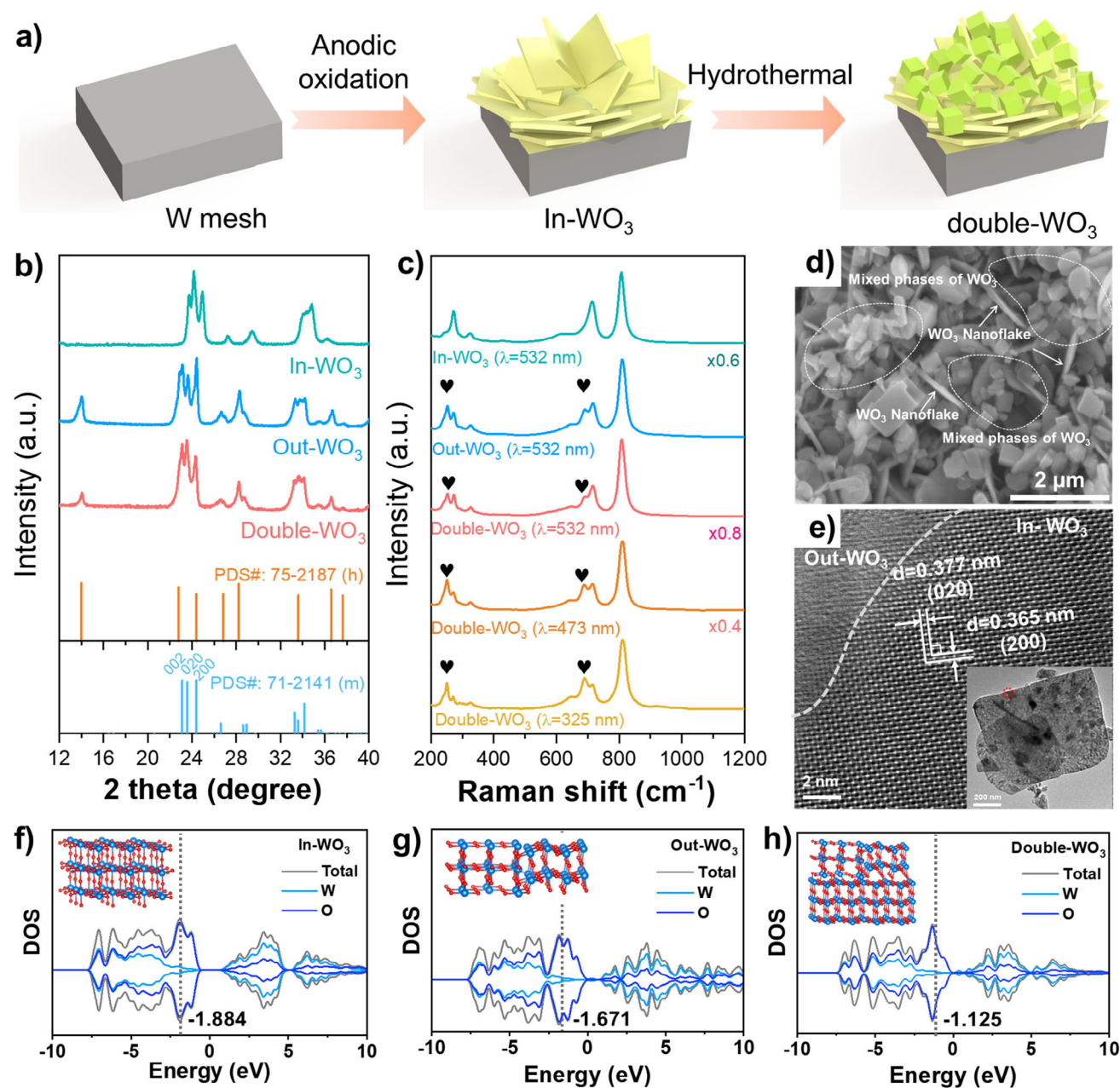


Figure 1. a) Schematic of the double-WO₃ photoelectrode preparation. b) XRD patterns. c) Raman spectra. d) SEM image of double-WO₃. e) High-resolution lattice structure of double-WO₃ (inset: HR-TEM image). f)–h) Theoretical models and DOS of in-WO₃ f), out-WO₃ g), and double-WO₃ h).

reveals the fastest charge transfer kinetics and most efficient electron-hole separation of double-WO₃. And Mott–Schottky (M–S) plots (Figure S7) derived from capacitance values show that double-WO₃ exhibits a much smaller slope compared to the single-layer structures, indicating a higher charge carrier density (N_D). The band structures of WO₃-based photoelectrodes (Figure S8) were analyzed using UV–vis absorption spectra (Figure S9) and ultraviolet photoemission spectroscopy (UPS, Figure S10), which was described in Figure S11.

Figure 2b shows that double-WO₃ exhibits the lowest steady-state PL intensity among the samples, indicating the suppressed carrier recombination.^[41] Time-resolved PL

(TR-PL) spectra show that double-WO₃ exhibits slightly slower fluorescent decay kinetics than that of in-WO₃ or out-WO₃ (Figure 2c). Fitting the TR-PL spectra with a triple-exponential decay function revealed that double-WO₃ exhibits a longer average carrier lifetime (10.89 ns) than in-WO₃ (7.02 ns) and out-WO₃ (6.78 ns), indicating more efficient charge separation in the bilayer structure. Therefore, more photogenerated charges in the double-WO₃/PEC system can participate in the degradation of fluorinated organic pollutants.

To investigate the electron extraction kinetics in WO₃-based photoelectrodes, transient photocurrent (TPC)

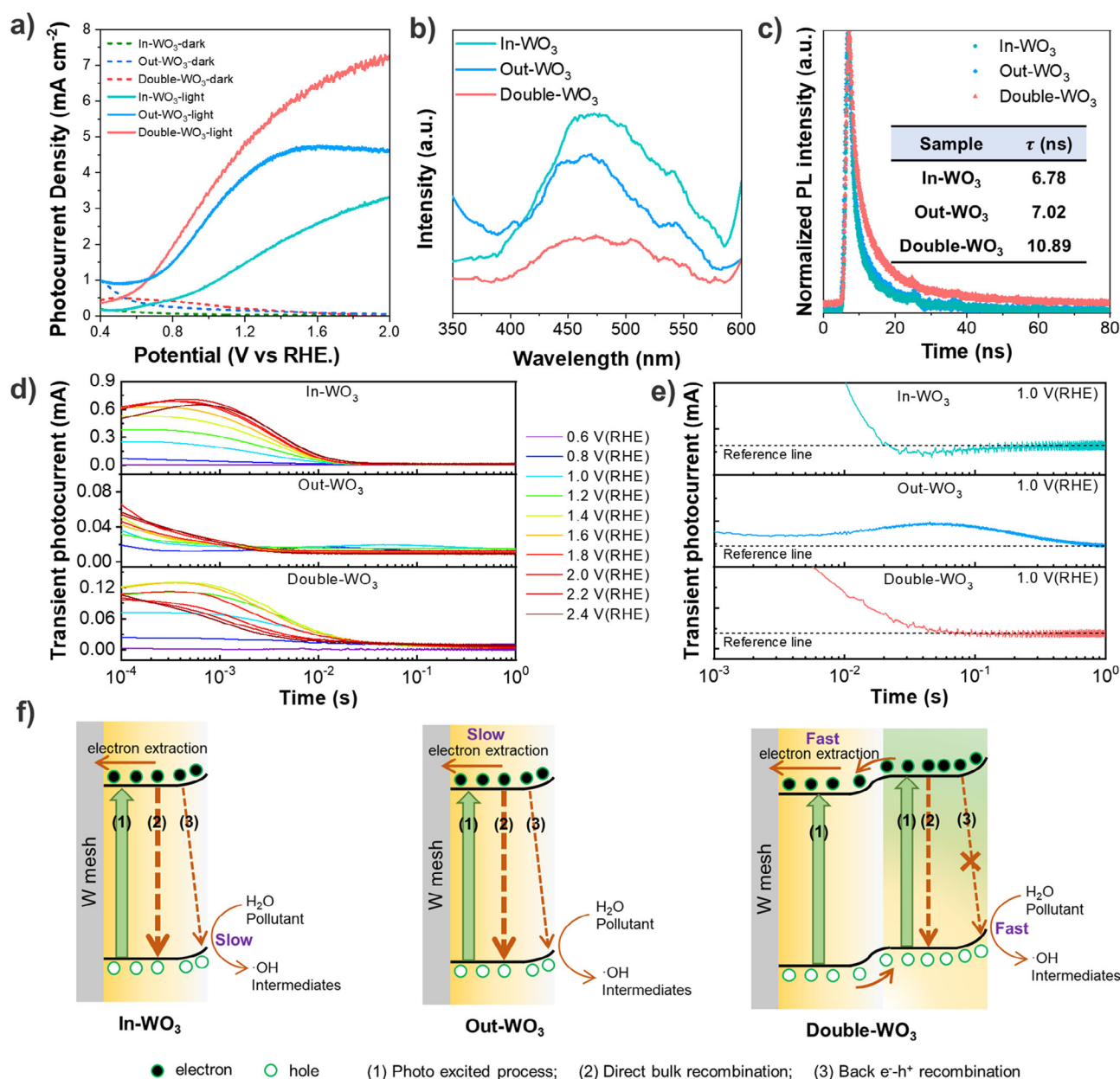


Figure 2. a) J - V curves under light illumination. b) PL spectra. c) Time-resolved PL spectra. d) Transient photocurrent response at different applied potentials (from 0.6 to 2.4 V_{RHE}) after laser excitation. e) Transient photocurrent response at 1.0 V_{RHE} over time. f) Schematic illustration of major charge carrier dynamics in WO₃-based photoelectrodes.

measurements were conducted at various applied potentials (Figure 2d). As the anodic bias increases, the transient photocurrent signals of in-WO₃, out-WO₃, and double-WO₃ rise simultaneously, indicating a greater density of long-lived photogenerated electrons being extracted into the external circuit.^[31] And double-WO₃ exhibits the highest extracted electron density. The strongest transient photocurrent response in double-WO₃ suggests that more photogenerated electron-hole pairs contribute to the PEC reaction compared to in-WO₃ and out-WO₃. The decay time associated with this transient photocurrent at different applied potentials represents the electron extraction kinetics of the samples.^[42] Specifically, in double-WO₃, the half-time reduces from

~19.7 ms to ~1 ms as the applied bias increases from 0.8 V_{RHE} to 2.4 V_{RHE} . In contrast, out-WO₃ shows slower electron extraction kinetics across the potential range. These findings confirm that introducing WO₃ nanoflakes as the ETL significantly accelerates electron extraction, highlighting the crucial role of in-WO₃ in enhancing overall PEC performance.

Since PEC degradation relies on the accumulation of multiple h⁺ at the photoanode surface, the kinetic competition between surface reactions and back electron-hole recombination can significantly impact PEC efficiency.^[24,32] To distinguish these competing behaviors, transient photocurrent responses of WO₃-based photoanodes were recorded at 1.0 V_{RHE} (Figure 2e). Notably, in-WO₃ exhibits a negative

transient current before returning to zero, whereas out-WO₃ and double-WO₃ do not show such behavior. This reverse electron flow at moderate applied potentials suggests electron backflow from the external circuit into the WO₃ photoelectrode due to delayed recombination. As illustrated in Figure 2f, this process involves i) charge separation, ii) hole accumulation at the surface while electrons diffuse into the circuit, and iii) bulk electron recombination with surface holes, inducing reverse electron flow.^[23,43] These findings indicate slow surface reaction kinetics in in-WO₃, whereas out-WO₃ and double-WO₃ exhibit significantly enhanced reaction rates. Thus, the double-WO₃ photoelectrode facilitates rapid electron extraction and efficient surface reactions, effectively suppressing electron-hole recombination.

The PEC degradation performance of fluorinated organic pollutants was evaluated using BPAF (structure shown in Table S1) as a representative pollutant (Figure 3). BPAF exhibited negligible self-photolysis under Xenon lamp irradiation without catalysts, and adsorption onto the photoelectrodes was minimal (Figure S12). As shown in Figure 3a, among the tested WO₃-based photoelectrodes, double-WO₃ exhibited the highest degradation efficiency (99.9%), significantly surpassing in-WO₃ and out-WO₃ (Figure 3a). The degradation rate constant of BPAF by double-WO₃ ($6.4 \times 10^{-2} \text{ min}^{-1}$) was approximately 2.9 and 2.4 times higher than those of in-WO₃ ($2.7 \times 10^{-2} \text{ min}^{-1}$) and out-WO₃ ($2.2 \times 10^{-2} \text{ min}^{-1}$), respectively (Figure 3b). Moreover, the TOC removal efficiency using double-WO₃ (57%) was also considerably higher (Figure S13), exceeding those of previously reported systems (Table S2). Besides, the system maintained high degradation efficiency even at 100 ppm of BPAF, highlighting its robustness and applicability in real wastewater treatment (Figure S14). Extending the reaction time further enhances BPAF degradation and mineralization (Figure 3c). After 9 h of PEC treatment using double-WO₃, the BPAF mineralization efficiency reaches nearly complete removal (Figure 3c). Notably, the TOC concentration decreases to 3.9 ppm within only 5 h, which meets the drinking water contamination standard (4 ppm) set by the US Environmental Protection Agency. Thus, the double-WO₃ photoelectrode demonstrates excellent performance for fluorinated pollutant degradation and mineralization.

To investigate the role of the ETL in double-WO₃, the effect of inner layer thickness on PEC degradation performance was evaluated (Figure 3d). As anodic oxidation time increased, the inner layer and overall film thickness also increased (Figures S15–S17). The PEC degradation rate initially improved with increasing thickness but declined beyond a certain point. The highest degradation rate (0.046 min^{-1}) was achieved with a film thickness of $\sim 1.5\text{--}2.5 \text{ }\mu\text{m}$. Optimal PEC performance occurred when WO₃ nanoflakes formed a monolayer ($\sim 1.8 \text{ }\mu\text{m}$) on the W substrate, which is because the monolayer of WO₃ nanoflakes greatly reduces the presence of grain boundaries, facilitating efficient transport of photoinduced electrons from WO₃ to the W substrate.^[14,31]

Comparative experiments under photocatalysis (PC) and electrocatalysis (EC) conditions were conducted to investigate the synergy between photo and electric energy in PEC degradation (Figures 3e and S18). The double-WO₃ electrode

exhibits a significantly higher BPAF degradation rate constant under PEC conditions ($4.2 \times 10^{-2} \text{ min}^{-1}$) compared to PC ($2.4 \times 10^{-2} \text{ min}^{-1}$) or EC ($2.2 \times 10^{-2} \text{ min}^{-1}$) conditions, confirming a strong synergistic effect. Similar trends were observed for in-WO₃ and out-WO₃ (Figure S19). Aiming to explore the synergistic effect of PC and EC, the PEC degradation processes are conducted under specific incident light with different wavelengths or various applied voltages subsequently (Figures S20–S21).

The cyclic BPAF degradation tests indicate that the double-WO₃ remains high degradation performance (91.4% of BPAF removal and 55.0% of TOC removal) for at least five cycles of PEC degradation tests (Figures 3f and S22). The SEM images of double-WO₃ photoelectrode after 5 cycles' reaction reveal that the catalyst exhibits no obvious change and uniformly distributes onto the substrate (Figure S23a). Besides, no new peaks have been detected in the XRD pattern of double-WO₃ after the reaction (Figure S23b). The above results imply excellent durability of the double-WO₃ photoelectrode.

The PEC degradation performance of WO₃-based photoelectrodes was further evaluated using typical fluorinated pollutants, including 4-fluorophenol (4-FP) and pentafluorophenol (PFP) (Figures 3g–i and S24). As seen from Figure 3g,h, although in-WO₃ and out-WO₃ exhibit decent degradation efficiencies for fluorinated pollutants (>90%), their mineralization and defluorination efficiencies remain relatively low (<50%). Specifically, double-WO₃ achieved over 99% degradation of 4-FP and PFP (Figure 3i) and exhibited notably higher TOC removal efficiencies compared to previously reported systems (Tables S3 and S4), reaching more than 99% TOC removal during PFP degradation within 150 min. Moreover, the defluorination efficiencies for BPAF, 4-FP, and PFP reached remarkably high values, demonstrating the effectiveness of C–F bond cleavage. These results confirm the superior universality and exceptional PEC performance of the double-WO₃ photoelectrode for the degradation and mineralization of fluorinated organic pollutants.

In previous studies, the degradation of organic pollutants via the PEC process has been mainly ascribed to the presence of ROS, including $\cdot\text{OH}$, $\cdot\text{O}_2^-$, as well as the oxidative holes (h^+).^[44] To comprehend the PEC degradation mechanism by the double-WO₃ photoelectrode, common radical scavengers (methanol (MeOH) for $\cdot\text{OH}$, 4-Hydroxy-TEMPO (TEMPOL) for $\cdot\text{O}_2^-$ and EDTA-2Na for h^+) were separately added into the system under typical reaction conditions.^[45] Obvious inhibiting effects of these three scavengers are found (Figure S25), indicating that $\cdot\text{OH}$, $\cdot\text{O}_2^-$, and h^+ collectively play important roles in the BPAF degradation. The degradation efficiency of BPAF decreases from 99.9% to 19.0%, 39.9% or 73.9% with the addition of MeOH, EDTA-2Na, or TEMPOL, respectively. The contribution of ROS to BPAF degradation follows the order: $\cdot\text{OH} > \text{h}^+ > \cdot\text{O}_2^-$ and $\cdot\text{OH}$ is the dominant oxidative species. The large amounts of $\cdot\text{OH}$ originate from the direct oxidation of H₂O by holes, while $\cdot\text{O}_2^-$ is generated via the reduction of dissolved O₂ in the electrolyte by electrons transferred from the counter electrode.^[46]

Electron paramagnetic resonance (EPR) spin trapping with 5,5-dimethyl-1-pyrroline N-oxide (DMPO) in the

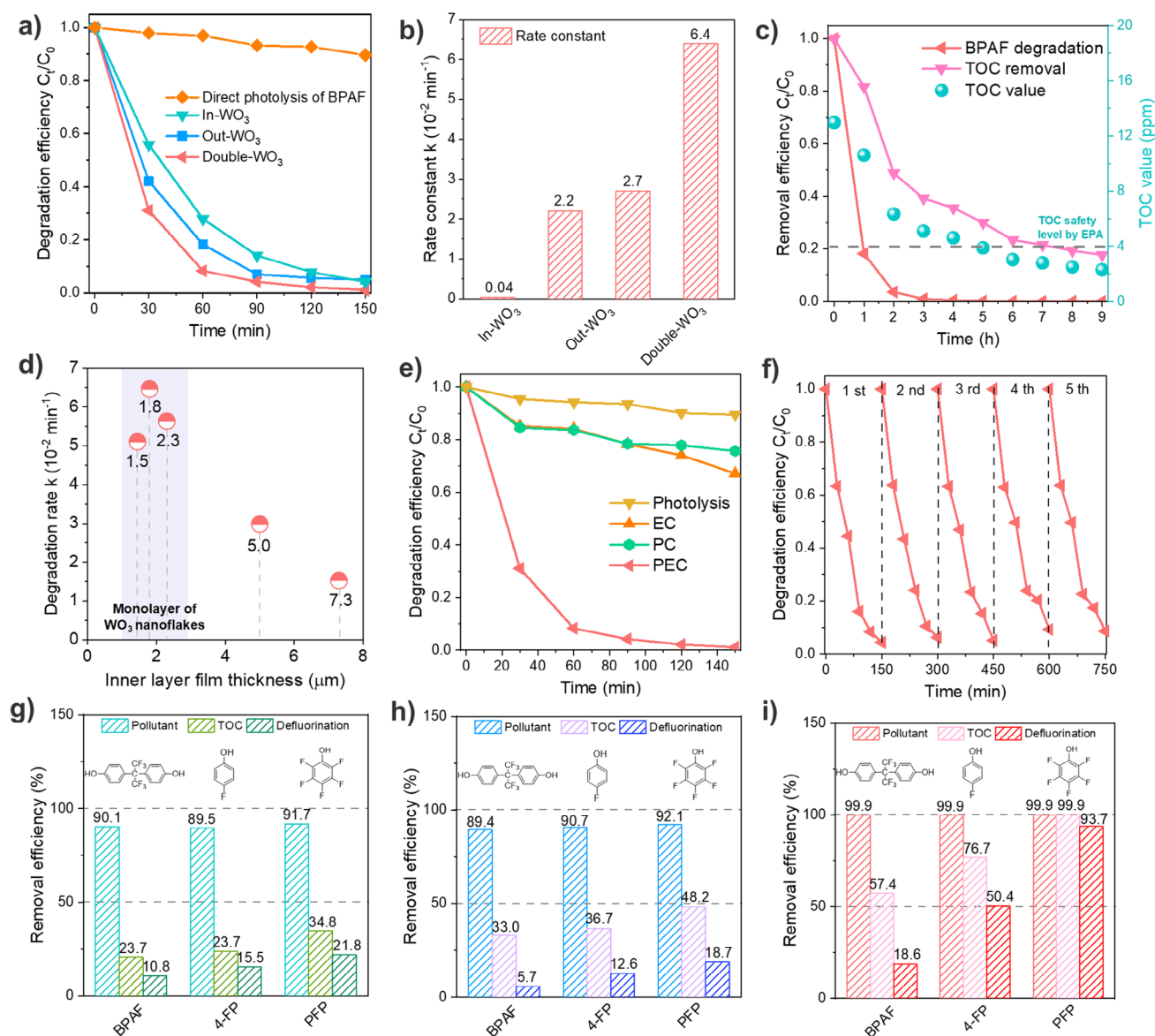


Figure 3. a) PEC degradation performance of BPAF by WO₃-based photoelectrodes. b) Corresponding degradation rate constants. c) TOC removal of BPAF by double-WO₃. d) Effect of inner layer thickness on PEC degradation of BPAF by double-WO₃. e) Comparative BPAF degradation by double-WO₃ under PC, EC, and PEC conditions. f) Cyclic PEC degradation by the double-WO₃. g)–i) PEC degradation, mineralization, and defluorination of fluorinated pollutants by in-WO₃ g), out-WO₃ h), and double-WO₃ i) after 150 min reaction.

WO₃-based photoelectrodes/PEC system confirms the existence of $\cdot\text{OH}$ (Figure 4a). The generated $\cdot\text{OH}$ is captured and evidenced by the four characteristic peaks with a peak strength of 1:2:2:1 of DMPO- $\cdot\text{OH}$. As shown, the characteristic EPR signal intensity of DMPO- $\cdot\text{OH}$ follows the order: double-WO₃ > out-WO₃ > in-WO₃, consistent with the scavenging experiments. Furthermore, TEMPO was employed as a spin-trapping agent to evaluate photogenerated h^+ (Figure 4b). After the reaction, the TEMPO-EPR intensity decreased significantly, with double-WO₃ showing the greatest intensity reduction among the three samples, indicating its higher generation and utilization of h^+ during the PEC process. Thus, double-WO₃ exhibits enhanced PEC degradation performance by effectively generating more ROS

and h^+ , confirming its superior catalytic activity toward fluorinated pollutant degradation.

Terephthalic acid (TA) was used as a fluorescence probe to monitor $\bullet\text{OH}$ generation via PL emission spectra (Figure S26).^[47] As shown, double-WO₃ exhibited the highest PL intensity, indicating the highest $\bullet\text{OH}$ formation rate via the PEC process. To further elucidate the degradation mechanism, the concentrations of oxidative species ($\cdot\text{OH}$, $\cdot\text{O}_2^-$, and h^+) were quantified based on PL, probe experiments, and EPR results (Figures 4c and S27–S29). Compared to in-WO₃ and out-WO₃, double-WO₃ demonstrated higher ROS concentrations due to improved charge separation and suppressed electron-hole recombination. Notably, $\bullet\text{OH}$ and $\bullet\text{O}_2^-$ concentrations followed the order

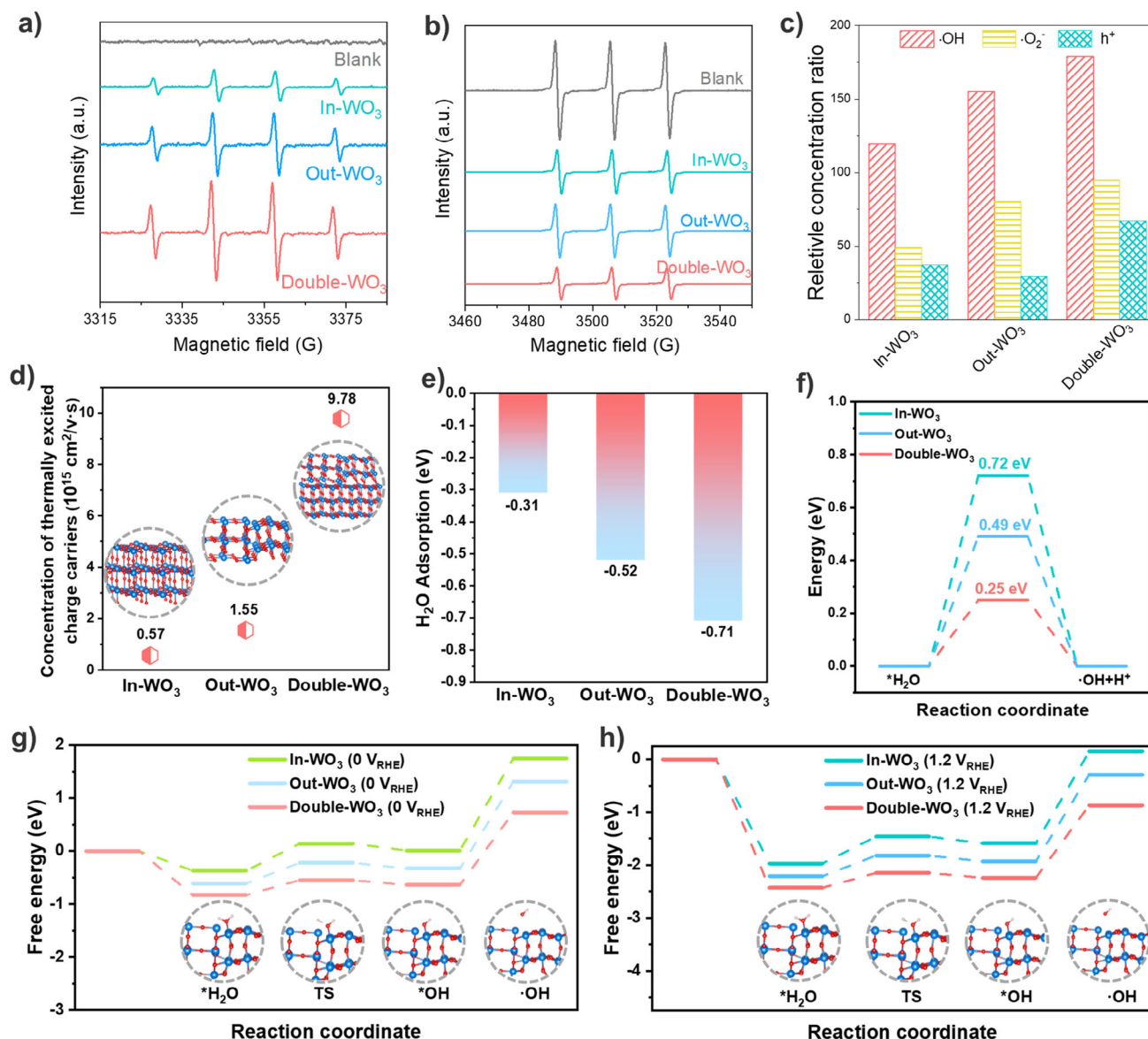


Figure 4. a) EPR spectra with DMPO added in the PEC process for 5 min. b) EPR spectra with TEMPO added in the PEC process for 5 min c) Relative concentration of ROS in WO₃-based PEC systems. d) Concentration of thermally excited charge carriers calculated by DFT. e) The calculated H₂O adsorption Gibbs free energy. f) Gibbs free energy of *OH intermediates. g) Comparison of free energy of different elementary steps in ·OH generation at 0 V_{RHE}. h) Comparison of free energy of different elementary steps in ·OH generation at 1.2 V_{RHE}.

double-WO₃ > out-WO₃ > in-WO₃, while h⁺ concentrations followed double-WO₃ > in-WO₃ > out-WO₃, attributed to the inner layer's rapid electron transport facilitating h⁺ accumulation. These variations in ROS concentrations likely play a crucial role in defluorination efficiency and degradation pathways of fluorinated pollutants.

In order to investigate the reasons for the variation in the electronic structure of the WO₃-based photoelectrodes, the DFT calculations were carried out naturally (Figure 4d). The concentration of thermally excited charge carriers of double-WO₃ is calculated to be $9.78 \times 10^{15} \text{ cm}^2 \text{ v}^{-1} \text{ s}^{-1}$, which is 17.1 and 6.3 times that of in-WO₃ ($5.7 \times 10^{14} \text{ cm}^2 \text{ v}^{-1} \text{ s}^{-1}$) and out-WO₃ ($1.55 \times 10^{15} \text{ cm}^2 \text{ v}^{-1} \text{ s}^{-1}$), agreeing well with the aforesaid results of photogenerated charge carrier dynamics. Taking experimental and theoretical calculations

into account, the results demonstrate that the construction of ETL and heterophase junctions can increase the concentration of excited charge carriers in a way that is beneficial for electron-hole pair separation and efficient charge carrier utilization, resulting in enhanced PEC performance toward degradation of fluorinated organic pollutants.

The Gibbs free energy of H₂O adsorption ($\Delta G_{\text{H}_2\text{O}^*}$) is a reliable descriptor for intrinsic H₂O activation, and a low $\Delta G_{\text{H}_2\text{O}^*}$ value can maximize H₂O oxidation performance.^[48] As displayed in Figure 4e, the $\Delta G_{\text{H}_2\text{O}^*}$ of double-WO₃ (-0.71 eV) was significantly lower compared to within-WO₃ (-0.31 eV) and out-WO₃ (-0.52 eV), indicating favorable H₂O adsorption kinetics on double-WO₃ during the PEC process. To further investigate the relationship between electronic structure and H₂O oxidation performance, Gibbs

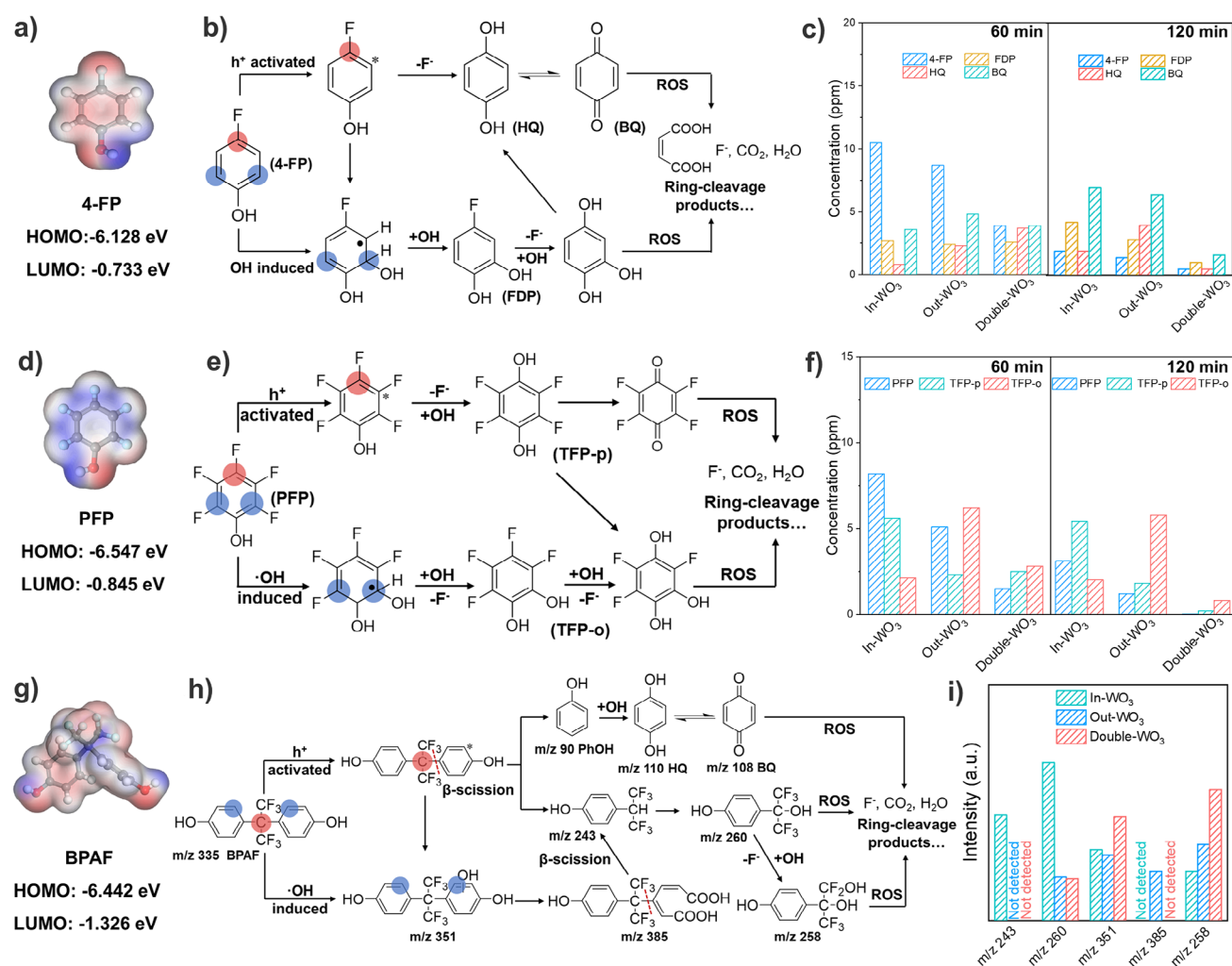


Figure 5. a) ESP of 4-FP. b) Possible degradation pathways of 4-FP in the PEC system. c) Concentration of main intermediates in PEC degradation of 4-FP. d) ESP of PFP. e) Possible degradation pathways of PFP in the PEC system. f) Concentration of main intermediates in PEC degradation of PFP. g) ESP of BPAF. h) Possible degradation pathways of BPAF in the PEC system. i) Concentration of main intermediates in PEC degradation of BPAF.

free energies for $\bullet\text{OH}$ intermediates were calculated. The primitive steps of the single electron-based H_2O oxidation process involved H_2O (H_2O adsorbed and activated by catalyst), $\bullet\text{OH}$ (the transition state of adsorbed- OH), and formation of $\bullet\text{OH}$, and thus the optimized models including H_2O , $\bullet\text{OH}$, and $\bullet\text{OH}$ are outlined in Figure 4f. As seen, the energy barrier of the rate-determining step (RDS) involving deprotonation from H_2O to $\bullet\text{OH}$ by double-WO₃ was significantly reduced to 0.31 eV compared with others, indicating that the double-WO₃ was more thermodynamically favorable for catalyzing H_2O oxidation to generate $\bullet\text{OH}$.^[49]

Figure 4g,h depicts the overall H_2O oxidation processes under different applied potentials. At 0 V_{RHE} , the free energy exhibited a continuous uphill trend as the H_2O oxidation process proceeded, and the double-WO₃ showed a lower energy requirement than in-WO₃ or out-WO₃, resulting in an enhanced $\bullet\text{OH}$ generation (Figure 4g). To drive the reactions, an equilibrium potential of 1.2 V_{RHE} was applied, and the overall energy barriers for $\bullet\text{OH}$ generation on the double-WO₃ were largely reduced with a downhill trend

compared with that of in-WO₃ or out-WO₃, thus the double-WO₃ displayed a superior $\bullet\text{OH}$ generation performance (Figure 5h). Compared with in-WO₃ and out-WO₃, double-WO₃ facilitated faster adsorption and activation of H_2O , forming reactive intermediates ($\bullet\text{H}_2\text{O}$) more efficiently. Subsequently, the deprotonation of these activated species ($\bullet\text{H}_2\text{O} \rightarrow \bullet\text{OH}$) produced abundant $\bullet\text{OH}$ radicals, thereby greatly enhancing the overall catalytic efficiency of the PEC degradation process.

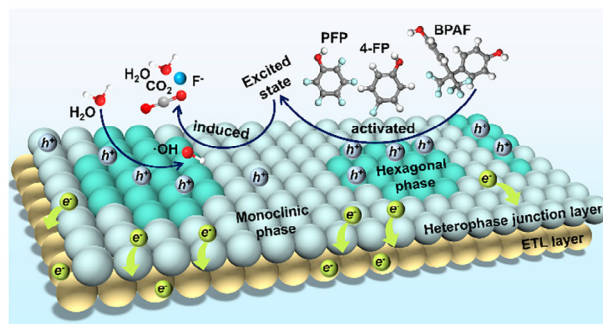
The degradation of fluorinated pollutants by in-WO₃, out-WO₃, and double-WO₃ confirms their effectiveness, though with varying defluorination and mineralization efficiencies. To clarify the mechanisms, ESP calculations, HPLC, and LC-MS/MS were used to propose possible PEC degradation pathways for 4-FP, PFP, and BPAF.

The ESP map, HOMO, and LUMO of 4-FP were computed using DFT (Figure 5a), which reveals that F and C atoms in the benzene ring have the lowest potential values, making them highly reactive toward ROS in the PEC system.^[50] Additionally, HOMO and LUMO distributions

(Figure S29a) indicate high electron density in the C–F bond and benzene ring, making them primary ROS attack sites.^[51] Based on HPLC and LC-MS/MS analyses, a PEC degradation pathway for 4-FP is proposed (Figures 5b and S30). The process follows two key pathways: 1) Photogenerated h^+ excites 4-FP, inducing C–F bond cleavage and forming F^- and hydroquinone (HQ), which is rapidly converted to benzoquinone (BQ) via an electron shuttle mechanism and further oxidized by $\bullet OH$, resulting in ring cleavage and the formation of 4-oxohex-2-enedioic acid. 2) $\bullet OH$ radicals attack the ortho-position of the hydroxyl group in 4-FP, forming fluoro-dihydroxyphenol (FDP), which undergoes further oxidation to 3-fluoro-4-hydroxyhexa-2,4-dienoic acid, eventually converting into low-molecular-weight intermediates (e.g., tartaric acid and succinic acid) and ultimately mineralizing into CO_2 , H_2O , and F^- . Intermediate analysis at 60 and 120 min (Figure 5c) showed complete degradation of FDP, HQ, and BQ in the double- WO_3 system, while these intermediates remained in the in- WO_3 and out- WO_3 systems, highlighting the superior mineralization efficiency of double- WO_3 .

Furthermore, the ESP analysis of PFP (Figures 5d and S29b) reveals that the –F and –OH groups in the benzene ring exhibit the lowest potential values, making them highly reactive toward ROS in the PEC system. Based on this and HPLC results, a PEC degradation pathway for PFP is proposed (Figures 5e and S31). During degradation, photogenerated holes preferentially attack the para-position C–F bond, leading to F^- substitution and the formation of tetrafluoroquinol (TFP-p), which is further converted into tetrafluorobenzoquinone and 2,3,5-trifluorobenzotriol. Meanwhile, $\bullet OH$ radicals selectively react with the ortho-position C–F bond, forming tetrafluorocatechol (TFP-o), which undergoes further defluorination to generate 2,3,5-trifluorobenzotriol. These intermediates are ultimately oxidized into CO_2 , H_2O , and F^- .^[52] Given the key roles of TFP-p and TFP-o in the PFP degradation pathway, their concentrations were monitored at 60 and 120 min (Figure 5f). In the in- WO_3 /PEC system, TFP-p was the main intermediate, indicating rapid electron transfer and h^+ accumulation that initiated PFP activation but limited further degradation due to insufficient ROS. In contrast, TFP-o was predominant in the out- WO_3 /PEC system, suggesting $\bullet OH$ -driven defluorination. Notably, no significant intermediate accumulation was observed in the double- WO_3 system, indicating efficient ROS generation and rapid PFP degradation following h^+ activation.

The ESP analysis of BPAF (Figures 5g and S29c) reveals that the C–F and –OH groups in the benzene ring have the lowest potential values, making them highly susceptible to ROS attack in the PEC system. Based on HPLC-MS/MS results, the BPAF degradation pathways by WO_3 -based photoelectrodes are proposed (Figures 5h and S32–S35). Similar to other fluorinated pollutants, BPAF follows two primary degradation pathways. In the first pathway, photogenerated holes induce β -cleavage of BPAF, forming a m/z 243 intermediate and phenol, which subsequently transforms into m/z 260 and m/z 258, along with benzoquinone (BQ) and hydroquinone (HQ). In the second pathway, $\bullet OH$ radicals drive a direct hydroxylation reaction, yielding a m/z 351



Scheme 1. Schematic mechanism of PEC degradation of fluorinated pollutants over double- WO_3 photoelectrode.

product. As degradation progresses, aromatic ring opening and multi-carboxylation convert the intermediates into m/z 385, which are further oxidized into low-molecular-weight intermediates and ultimately mineralized into CO_2 , H_2O , and F^- . To assess degradation efficiency, key intermediates after 90 min of PEC degradation were analyzed (Figure 5i). The double- WO_3 /PEC system produced significantly fewer persistent intermediates compared to the in- WO_3 and out- WO_3 systems, indicating more efficient mineralization. Notably, m/z 243 was exclusively detected in the In- WO_3 system, likely due to efficient electron transfer by the ETL, which led to hole accumulation and BPAF activation. In contrast, m/z 385 appeared only in the Out- WO_3 system, suggesting its formation was primarily driven by $\bullet OH$ -mediated oxidation. Therefore, double- WO_3 outperformed in- WO_3 and out- WO_3 in defluorination and mineralization efficiency while minimizing persistent intermediates, underscoring the crucial roles of photogenerated holes and $\bullet OH$ in C–F bond cleavage and pollutant degradation.

Based on the above findings, a detailed degradation mechanism is proposed and illustrated in Scheme 1. Under light irradiation, the double- WO_3 photoelectrode generates electron-hole pairs, which are efficiently separated by an applied bias. The outer layer, with its hexagonal-monoclinic phase junction, enhances charge separation via a built-in electric field, while the inner layer acts as the ETL, facilitating rapid electron extraction to the substrate. These structural advantages enable efficient charge separation, fast surface reaction kinetics, and minimal electron-hole recombination, ensuring more photogenerated h^+ and ROS participate in the PEC process. In this process, h^+ preferentially activates fluorinated pollutants to an excited state, where C–F bonds become more susceptible to attack by $\bullet OH$ and other ROS. This facilitates C–F bond cleavage, leading to the formation of reactive intermediates, which are further oxidized into CO_2 , H_2O , and F^- under strong oxidative conditions.

Conclusion

In summary, a bilayer WO_3 photoelectrode (double- WO_3) with an electron transport layer and a heterophase junction was successfully fabricated on W mesh, demonstrating exceptional efficiency in degrading fluorinated organic pollutants.

Compared to in-WO₃ and out-WO₃, double-WO₃ exhibited superior PEC performance, achieving a high photocurrent density (4.3 mA cm⁻² at 1.2 V_{RHE}), 99.9% degradation of BPAF, 4-FP, and PFP, and nearly complete mineralization of PFP within 150 min. Under light irradiation, the built-in electric field in the outer layer enhances charge separation, while the ETL in the inner layer facilitates rapid electron extraction, reducing electron-hole recombination. These structural advantages boost charge separation, accelerate surface reactions, and enhance ROS generation. Consequently, photogenerated h⁺ activates fluorinated pollutants, making C–F bonds more susceptible to •OH attack, leading to efficient defluorination and mineralization into CO₂, H₂O, and F⁻. This study provides valuable insights into the mechanisms governing PEC degradation efficiency while offering a promising strategy for designing advanced PEC systems to remediate persistent fluorinated contaminants.

Experimental Section

The experimental section is provided in [Supporting Information](#).

Acknowledgements

This work was supported by the Fundamental Research Funds for the Central Universities (Lzujbky-2021-kb18) and National Natural Science Foundation of China (No. 42407534).

Conflict of Interests

The authors declare no conflict of interest.

Data Availability Statement

The data that support the findings of this study are available from the corresponding author upon reasonable request.

Keywords: Bilayer WO₃ photoelectrode • Electron transport layer • Fluorinated organic pollutants • Photoelectrocatalytic degradation mechanism

- [1] J. Han, L. Kiss, H. Mei, A. M. Remete, M. Ponikvar-Svet, D. M. Sedgwick, R. Roman, S. Fustero, H. Moriwaki, V. A. Soloshonok, *Chem. Rev.* **2021**, *121*, 4678–4742.
- [2] Y. Zhi, X. Lu, G. Munoz, L. W. Y. Yeung, A. O. De Silva, S. Hao, H. He, Y. Jia, C. P. Higgins, C. Zhang, *Environ. Sci. Technol.* **2024**, *58*, 21393–21410.
- [3] W. Luo, K. Liu, T. Luo, J. Fu, H. Zhang, C. Ma, T.-S. Chan, C.-W. Kao, Z. Lin, L. Chai, M. L. Coote, M. Liu, *J. Am. Chem. Soc.* **2025**, *147*, 7391–7399.
- [4] H. Chi, W. Wang, J. Ma, R. Duan, C. Ding, R. Song, C. Li, *Chin. J. Catal.* **2023**, *55*, 171–181.

- [5] X. Liu, A. Sau, A. R. Green, M. V. Popescu, N. F. Pompetti, Y. Li, Y. Zhao, R. S. Paton, N. H. Damrauer, G. M. Miyake, *Nature* **2025**, 637, 601–607.
- [6] Z. Chen, J. Wang, B. Yang, J. Li, Z. Liang, X. Liu, Y. Bao, J. Cao, M. Xing, *Nat. Water* **2025**, *3*, 334–344.
- [7] J. Wang, K. Liu, W. Liao, Y. Kang, H. Xiao, Y. Chen, Q. Wang, T. Luo, J. Chen, H. Li, T.-S. Chan, S. Chen, E. Pensa, L. Chai, F. Liu, L. Jiang, C. Liu, J. Fu, E. Cortés, M. Liu, *Nat. Catal.* **2025**, *8*, 229–238.
- [8] J. Ma, K. Mao, J. Low, Z. Wang, D. Xi, W. Zhang, H. Ju, Z. Qi, R. Long, X. Wu, L. Song, Y. Xiong, *Angew. Chem. Int. Ed.* **2021**, *60*, 9357–9361.
- [9] M. S. Koo, X. Chen, K. Cho, T. An, W. Choi, *Environ. Sci. Technol.* **2019**, *53*, 9926–9936.
- [10] K. Dang, L. Wu, S. Liu, S. Zhao, Y. Zhang, J. Zhao, *Angew. Chem. Int. Ed.* **2025**, n/a, e202423457.
- [11] F. Kang, Q. Wang, D. Du, L. Wu, D. W. F. Cheung, J. Luo, *Angew. Chem. Int. Ed.* **2025**, *64*, e202417648.
- [12] W. Kong, X. Zhang, S. Liu, Y. Zhou, B. Chang, S. Zhang, H. Fan, B. Yang, *Adv. Mater. Interfaces* **2019**, *6*, 1801653.
- [13] Q. Wang, L. I. Oldham, A. Giner-Requena, Z. Wang, D. Benetti, S. Montilla-Verdú, R. Chen, D. Du, T. Lana-Villarreal, U. Aschauer, N. Guijarro, J. R. Durrant, J. Luo, *J. Am. Chem. Soc.* **2024**, *146*, 34681–34689.
- [14] F. Kong, H. Zhou, Z. Chen, Z. Dou, M. Wang, *Angew. Chem. Int. Ed.* **2022**, *61*, e202210745.
- [15] M. Ma, K. Zhang, P. Li, M. S. Jung, M. J. Jeong, J. H. Park, *Angew. Chem. Int. Ed.* **2016**, *55*, 11819–11823.
- [16] T. H. Jeon, D. Monllor-Satoca, G. H. Moon, W. Kim, H. I. Kim, D. W. Bahnemann, H. Park, W. Choi, *Nat. Commun.* **2020**, *11*, 967.
- [17] M. Xiao, B. Luo, Z. Wang, S. Wang, L. Wang, *Sol. RRL* **2020**, *4*, 1900509.
- [18] A. Li, Z. Wang, H. Yin, S. Wang, P. Yan, B. Huang, X. Wang, R. Li, X. Zong, H. Han, C. Li, *Chem. Sci.* **2016**, *7*, 6076–6082.
- [19] X. Wang, S. Jin, H. An, X. Wang, Z. Feng, C. Li, *J. Phys. Chem. C* **2015**, *119*, 22460–22464.
- [20] Q. Ma, R. Song, F. Ren, H. Wang, W. Gao, Z. Li, C. Li, *Appl. Catal., B* **2022**, *309*, 121292.
- [21] X. Wang, Q. Xu, M. Li, S. Shen, X. Wang, Y. Wang, Z. Feng, J. Shi, H. Han, C. Li, *Angew. Chem. Int. Ed.* **2012**, *51*, 13089–13092.
- [22] R. Chen, F. Fan, C. Li, *Angew. Chem. Int. Ed.* **2022**, *61*, e202117567.
- [23] K. George, T. Khachatryan, M. van Berkel, V. Sinha, A. Bieberle-Hütter, *ACS Catal.* **2020**, *10*, 14649–14660.
- [24] S. Liu, L. Wu, D. Tang, J. Xue, K. Dang, H. He, S. Bai, H. Ji, C. Chen, Y. Zhang, J. Zhao, *J. Am. Chem. Soc.* **2023**, *145*, 23849–23858.
- [25] H. Ge, L. Zheng, G. Yuan, W. Shi, J. Liu, Y. Zhang, X. Wang, *J. Am. Chem. Soc.* **2024**, *146*, 10735–10744.
- [26] C. Ding, Z. Wang, J. Shi, T. Yao, A. Li, P. Yan, B. Huang, C. Li, *ACS Appl. Mater. Interfaces* **2016**, *8*, 7086–7091.
- [27] O. Zandi, J. A. Beardslee, T. Hamann, *J. Phys. Chem. C* **2014**, *118*, 16494–16503.
- [28] T. Hisatomi, H. Dotan, M. Stefiik, K. Sivula, A. Rothschild, M. Grätzel, N. Mathews, *Adv. Mater.* **2012**, *24*, 2699–2702.
- [29] E. Kim, S. Kim, Y. M. Choi, J. H. Park, H. Shin, *ACS Sustain. Chem. Eng.* **2020**, *8*, 11358–11367.
- [30] W. Li, P. Da, Y. Zhang, Y. Wang, X. Lin, X. Gong, G. Zheng, *ACS Nano* **2014**, *8*, 11770–11777.
- [31] S. Corby, L. Francàs, S. Selim, M. Sachs, C. Blackman, A. Kafizas, J. R. Durrant, *J. Am. Chem. Soc.* **2018**, *140*, 16168–16177.
- [32] F. L. e Formal, S. R. Pendlebury, M. Cornuz, S. D. Tilley, M. Grätzel, J. R. Durrant, *J. Am. Chem. Soc.* **2014**, *136*, 2564–2574.

- [33] L. Steier, I. Herraiz-Cardona, S. Gimenez, F. Fabregat-Santiago, J. Bisquert, S. D. Tilley, M. Grätzel, *Adv. Funct. Mater.* **2014**, *24*, 7681–7688.
- [34] M. Sun, R.-T. Gao, J. He, X. Liu, T. Nakajima, X. Zhang, L. Wang, *Angew. Chem. Int. Ed.* **2021**, *60*, 17601–17607.
- [35] P. Zhang, Z. Tian, Y. Kang, B. He, Z. Zhao, C.-T. Hung, L. Duan, W. Chen, Y. Tang, J. Yu, L. Mai, Y.-F. Li, W. Li, D. Zhao, *J. Am. Chem. Soc.* **2022**, *144*, 20964–20974.
- [36] H. Qi, J. Wolfe, D. Wang, H. J. Fan, D. Fichou, Z. Chen, *Nanoscale* **2014**, *6*, 13457–13462.
- [37] C. Santato, M. Odziemkowski, M. Ulmann, J. Augustynski, *J. Am. Chem. Soc.* **2001**, *123*, 10639–10649.
- [38] X. Wang, C. Li, *J. Phys. Chem. C* **2018**, *122*, 21083–21096.
- [39] S. Wang, H. Chen, G. Gao, T. Butburee, M. Lyu, S. Thaweesak, J.-H. Yun, A. Du, G. Liu, L. Wang, *Nano Energy* **2016**, *24*, 94–102.
- [40] D. Hu, P. Diao, D. Xu, M. Xia, Y. Gu, Q. Wu, C. Li, S. Yang, *Nanoscale* **2016**, *8*, 5892–5901.
- [41] F. Amano, D. Li, B. Ohtani, *Chem. Commun.* **2010**, *46*, 2769.
- [42] Y. P. Xie, G. Liu, L. Yin, H.-M. Cheng, *J. Mater. Chem.* **2012**, *22*, 6746.
- [43] P. S. Shinde, X. Peng, J. Wang, Y. Ma, L. E. McNamara, N. I. Hammer, A. Gupta, S. Pan, *ACS Appl. Energy Mater.* **2018**, *1*, 2283–2294.
- [44] S. Garcia-Segura, E. Brillas, *J. Photochem. Photobiol., C* **2017**, *31*, 1–35.
- [45] Z.-H. Xie, C.-S. He, H.-Y. Zhou, L.-L. Li, Y. Liu, Y. Du, W. Liu, Y. Mu, B. Lai, *Environ. Sci. Technol.* **2022**, *56*, 8784–8795.
- [46] M. S. Koo, K. Cho, J. Yoon, W. Choi, *Environ. Sci. Technol.* **2017**, *51*, 6590–6598.
- [47] S.-L. Xu, W. Wang, H.-T. Li, Y.-X. Gao, Y. Min, P. Liu, X. Zheng, D.-F. Liu, J.-J. Chen, H.-Q. Yu, X. Zhou, Y. Wu, *Adv. Mater.* **2025**, *37*, 2500371.
- [48] H. Jia, N. Yao, C. Yu, H. Cong, W. Luo, *Angew. Chem. Int. Ed.* **2023**, *62*, e202313886.
- [49] S. Xue, C. Wei, M. Shen, X. Liang, J. Wang, C. Yang, W. Xing, S. Wang, W. Lin, Z. Yu, Y. Hou, J. C. Yu, X. Wang, *Proc. Natl. Acad. Sci. USA* **2024**, *121*, e2319751121.
- [50] F. Xiao, Z. Wang, J. Fan, T. Majima, H. Zhao, G. Zhao, *Angew. Chem. Int. Ed.* **2021**, *60*, 10375–10383.
- [51] L. Zhu, J. Ji, J. Liu, S. Mine, M. Matsuoka, J. Zhang, M. Xing, *Angew. Chem. Int. Ed.* **2020**, *59*, 13968–13976.
- [52] H. Chi, J. Ma, R. Duan, A. Wang, Y. Qiao, W. Wang, C. Li, *Water Res.* **2024**, *262*, 122101.

Manuscript received: March 19, 2025

Revised manuscript received: April 01, 2025

Accepted manuscript online: April 02, 2025

Version of record online: May 08, 2025